Article

Diphenyl Diselenide and SARS-CoV-2: *in silico* Exploration of the Mechanisms of Inhibition of Main Protease (M^pro) and Papain-like Protease (PL^pro)

Folorunsho Bright Omage, Andrea Madabeni, Amanda Resende Tucci, Pablo Andrei Nogara, Marco Bortoli, Alice dos Santos Rosa, Vivian Neuza dos Santos Ferreira, João Batista Teixeira Rocha, Milene Dias Miranda,* and Laura Orian*

ACCESS | 📊 Metrics & More | 📄 Article Recommendations | 🔵 Supporting Information

ABSTRACT: The SARS-CoV-2 pandemic has prompted global efforts to develop therapeutics. The main protease of SARS-CoV-2 (M^pro) and the papain-like protease (PL^pro) are essential for viral replication and are key targets for therapeutic development. In this work, we investigate the mechanisms of SARS-CoV-2 inhibition by diphenyl diselenide $(PhSe)_2$ which is an archetypal model of diselenides and a renowned potential therapeutic agent. The *in vitro* inhibitory concentration of $(PhSe)_2$ against SARS-CoV-2 in Vero E6 cells falls in the low micromolar range. Molecular dynamics (MD) simulations and density functional theory (DFT) calculations [level of theory: SMD-B3LYP-D3(BJ)/6-311G(d,p), cc-pVTZ] are used to inspect non-covalent inhibition modes of both proteases via π-stacking and the mechanism of covalent $(PhSe)_2$ + M^pro product formation involving the catalytic residue C145, respectively. The *in vitro* CC_{50} (24.61 μM) and EC_{50} (2.39 μM) data indicate that $(PhSe)_2$ is a good inhibitor of the SARS-CoV-2 virus replication in a cell culture model. The *in silico* findings indicate potential mechanisms of proteases' inhibition by $(PhSe)_2$; in particular, the results of the covalent inhibition here discussed for M^pro, whose thermodynamics is approximatively isoergonic, prompt further investigation in the design of antiviral organodiselenides.
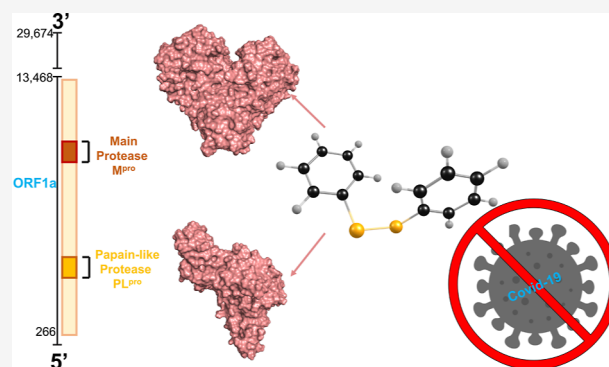
1. INTRODUCTION

The SARS-CoV-2 main and papain-like proteases, M^pro and PL^pro, are essential targets in the fight against this virus because they play a key role for its replication. These proteases have no equivalent enzymatic analogues in humans and thus no similar cleavage specificity, implying that their inhibition will likely have low toxicity.[1−3]

Recent events have shown a sudden increase in the number of variants with Omicron bearing the largest number of mutations.[4] Interestingly, no mutations have been observed in the conserved catalytic dyad/triad of M^pro/PL^pro, suggesting that an effective antiviral drug against SARS-CoV-2 targeting these proteases is a promising pharmacological strategy.[5]

Based on the recent literature, the inhibitory effects of SARS-CoV-2 M^pro and PL^pro by the popular organoselenide ebselen are explained by the formation of a selenylsulfide (Se−S) involving C145.[2,5−11] Besides the direct interaction with the catalytic C145, Menéndez et al. suggested that the inhibition of M^pro by ebselen may also be related to the interaction between protein domains II and III, a region which is essential for the dimerization of the protease.[12] Other aspects that remain almost unexplored are the potential interaction of organo-

selenium compounds with other residues, including cysteinyl residues not located in the active site, and with metabolites of ebselen.[13]

The catalytic sites of M^pro and PL^pro show strong similarity: the former protease has a catalytic dyad (H41 and C145), while the latter has a catalytic triad (C111, H272, and D286).[11] The protonation state of cysteine and histidine residues before nucleophilic attack on substrates was investigated for M^pro using different computational approaches (cluster-DFT, QM/MM, and a thorough MD study), which revealed that the couple of residues is more stable in the neutral state than in the zwitterionic form.[6,14−16] The activation of the catalytic dyad/triad (through a proton transfer from the C to the H residue) promotes the nucleophilic attack on the carbonyl carbon atom of a peptide

Journal of Chemical Information and Modeling
pubs.acs.org/jcim
Article

Scheme 1. (A) M^{pro} and (B) PL^{pro} Acylation and Deacylation Steps Involving Hydrolysis and Recovery of Reactant Complexes. (C) Proposed Mechanism of Covalent Inhibition of SARS-CoV-2 M^{pro} and (D) PL^{pro} by (PhSe)$_2$
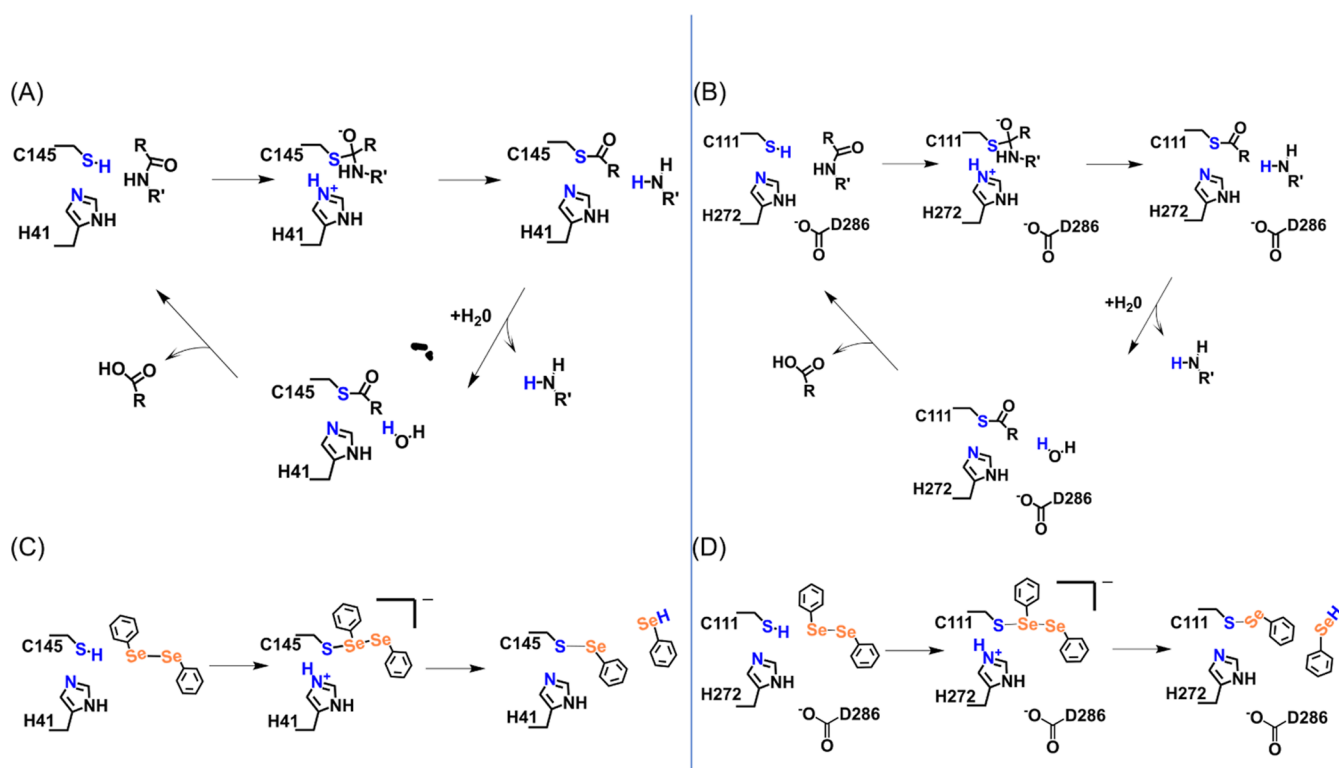
bond of the substrate by the sulfur atom of C145(S-)/C111(S-) (Scheme 1A,B), thus leading to a tetrahedral thiohemiketal (THA) intermediate.[17] The cleavage of the peptide bond occurs via a back proton transfer from the protonated H41/H272 to the nitrogen atom of the substrate. The peptide is released from the active site as a water molecule that attacks the carbonyl carbon atom of the peptide, together with the proton transfer to H41/H272 (Scheme 1A,B). The covalent bond between C145 and the peptide of this protonated intermediate is then broken to release the second product of the reaction in the deacylation phase, and the zwitterion is finally neutralized.

In the presence of an organoselenium ligand, the formation of a covalent S−Se bond with C145/C111 interrupts the normal C-protease activity (Scheme 1C,D),[17] as the inhibitor–enzyme complex formed by covalently bonded molecules such as ebselen and analogues hampers the subsequent steps in the cycle.[6,14,18]

The PL^{pro} active site has a canonical Cys protease catalytic triad (C111, H272, and D286), while M^{pro} has a catalytic dyad (C145 and H41 residues).[19,20] In PL^{pro}, C111 acts as a nucleophile by cleaving the substrate peptide bond, and H272 and D286 residues act as an acid−base pair promoting the thiol (Cys) deprotonation and thus enhancing its nucleophilicity.[21,22] Therefore, D286 is essential for PL^{pro} catalytic activity. On the other hand, M^{pro} has a catalytic dyad, and the proton transfer occurs between C145 and H41. H41 presents a hydrogen bond with a water molecule, which also has a hydrogen bond with the side chain of D187. However, D187 interacts with the R40 residue by a strong salt bridge.[20] Thus, in M^{pro}, the role of D187 is more structural than catalytic.

Diselenides are an important class of organoselenium compounds that have been studied mainly for their antioxidant

and anti-inflammatory potential.[23−26] (PhSe)$_2$ is the parent compound of diaryl diselenides and displays weak electrophilic potential.[27,28] Conversely, in terms of electrophilicity, ebselen, which is a selenenylamide, possesses strong electrophilic potential.[29] The toxicological and pharmacological interaction of (PhSe)$_2$ with different targets has been studied *in silico*[13,24,30−33] and *in vitro*,[34] and antiviral[9,35] and antifungal activity[36] was reported. Thus, (PhSe)$_2$ is interesting because it represents an archetypal model or scaffold of diselenide compounds and because it is a renowned potential therapeutic agent with inhibitory potency against M^{pro} in the low micromolar range and, consequently, has pharmacological significance.[23] Of pharmacological significance, the plasmatic concentration of (PhSe)$_2$ after oral administration of relatively high doses to rodents is in the micromolar range.[7,23,37] In this work, after verifying the *in vitro* (PhSe)$_2$ effect against SARS-CoV-2 replication, we sought a possible mechanism of action through an *in silico* approach. For this purpose, we thoroughly analyze *in silico* the structural and chemical mechanism of SARS-CoV-2 proteases' inhibition by (PhSe)$_2$, employing molecular docking, molecular dynamics (MD), and density functional theory (DFT) protocols. After docking the ligand, the non-covalent complex of (PhSe)$_2$ with M^{pro} and PL^{pro} is generated by MD simulation of the equilibrated system. DFT calculations are used to investigate the plausible mechanistic reaction steps taking place in the active site cluster; this approach has been carried out only for (PhSe)$_2$ + M^{pro}.

2. MATERIALS AND METHODS

2.1. *in vitro* Assays. All the tested compounds were resuspended in 100% dimethyl sulfoxide (DMSO) for the *in vitro* assays, aliquoted, and stored at −20 °C. A maximum of three freezing and thawing cycles were performed to maintain

chemical stability and avoid compound degradation.[38] In fact, $(PhSe)_2$ is very stable in DMSO solution when kept at 8 °C for more than 1 month (unpublished results). In the assays, the DMSO final concentrations were equal to or lower than 0.1% (v/v) when diluted in Dulbecco's modified Eagle's medium (DMEM-Gibco), not affecting the growth of the cells.[39,40]

Vero E6 cells (*Cercopithecus aethiops*; kidney epithelial) were infected with the SARS-CoV-2 isolate (GISAID EPI ISL #414045) in multiplicity of infection (MOI) 0.01 using DMEM with 0.01% N-2-hydroxyethylpiperazine-N'-2-ethane-sulfonic acid (Gibco). After 1 h, the supernatants were harvested, and the cells were incubated with $(PhSe)_2$ at different concentrations (from 0.78 to 12 μM). After 24 h of infection, the supernatants were removed and the virus titrated by plaque forming unit assay (PFU/mL).[41,42]

For PFU assay, monolayers of Vero E6 cells (2×10^4 cells/well) in 96-well plates were exposed to 50 μL of supernatant dilutions for 1 h at 37 °C in 5% CO_2. After this, 50 μL of semisolid high-glucose DMEM containing 2% fetal bovine serum and 2.4% carboxymethylcellulose (CMC) was added, and cultures were incubated for 3 days at 37 °C. Then, the cells were fixed with 100 μL of 10% formalin for 3 h at room temperature. The cell monolayer was stained with 0.04% solution of crystal violet in 20% ethanol for 1 h, and PFUs were counted. The virus titers were determined by PFU/mL.[42]

All procedures related to virus culture were handled at a biosafety level 3 (BSL3) multiuser facility, according to WHO guidelines.[43]

For cytotoxicity analysis, monolayers of Vero E6 (10^4 cells/well) in 96-well plates were treated for 72 h with different concentrations of all compounds tested. Then, 5 mg/mL 3-(4,5-dimethylthiazol-2-yl)-2,5-diphenyltetrazolium bromide (MTT—Sigma) in 1X phosphate buffered saline (PBS) was added to the cells, according to manufacturer's instructions. After 2 h at 37 °C, 10% sodium dodecyl sulfate was added. After incubating for 2 h at 37 °C, the plates were read in a spectrophotometer at 570 nm.

All experiments were carried out at least three independent times, including a minimum of two technical replicates in each assay. The dose–response curves used to calculate the EC_{50} and CC_{50} values were generated by a variable slope plot from Prism GraphPad software 8.0. The equations used to fit the best curve were generated based on R^2 values ≥ 0.9.

2.2. *in silico* Investigation. *2.2.1. System Preparation and Molecular Docking.* AutoDock Vina software[44,45] was used to simulate the binding pose of $(PhSe)_2$ with M^{pro} (PDB ID 6LU7[2]) and PL^{pro} (PDB ID 7JN2). The water of crystallization, ions, and ligands were removed during preparation, while the hydrogen atoms were added using the CHIMERA program; 100 steps of energy minimization (amberff99SB) followed.[46] Both the catalytic dyad and triad were considered neutral, as previously reported.[47,48] The M^{pro}'s grid box was centered at xyz coordinates of −14.04, 17.44, and 66.22, with box sizes of 25, 35, and 25 Å. PL^{pro} was located in a $20 \times 20 \times 20$ Å cubic box centered at xyz coordinates of 39.64, 30.68, and 1.66. For each ligand–receptor complex, 20 $(PhSe)_2$ binding poses were generated. The lowest binding free energies for M^{pro} and PL^{pro} were found to be −6.2 and −4.9 kcal mol^{-1}, respectively. The best Se–S(C) orientation was chosen as the binding pose model and used as the starting point in the MD simulations.

2.2.2. Molecular Dynamics (MD) Simulations. The AMBER 20[49] pmemd.cuda engine was used to perform all

MD simulations in explicit water. The residue numbering used in our study is identical to that used in the 6LU7 PDB file for M^{pro}; for PL^{pro}, numbering begins with residue 4 as obtained from the 7JN2 PDB file, which was reassigned as 1 during file preparation for simulation using pdb4amber. The AMBER ff14SB force field[50] was used for the proteases, while the general amber force field (GAFF) parameters for $(PhSe)_2$ were taken from the work by Torsello et al.[51]

For completeness, the set of parameters for this ligand is reported in the Supporting Information (Tables 1 S1). For the

Table 1. $(PhSe)_2$ Inhibition Activity in Vero E6 Cells

	Vero E6		
molecules	$CC_{50}{}^a$ (μM)	$EC_{50}{}^b$ (μM)	SI^c(CC_{50}/EC_{50})
$(PhSe)_2$	24.61 ± 4.55	2.39 ± 1.51	10.30

$^a CC_{50}$, the concentration required to reduce normal, non-infected cell viability by 50%. Values represent the mean ± SEM of duplicate samples from three independent experiments. $^b EC_{50}$, the concentration required to reduce inhibition of viral infection-induced cytopathogenicity by 50%. Values represent the mean ± SEM of duplicate samples from three independent experiments. $^c SI$, selectivity index determined by the ratio between CC50 and EC50.

zinc finger of PL^{pro}, the zinc AMBER force field (ZAFF) was used.[52] For PL^{pro}, the tetravalent binding site for Zn^{2+} is formed by C189, C192, C224, and C226 and was thus treated as Zn-CCCC using the ZAFF.

Each protease with the diselenide ligand was solvated in a truncated octahedral water box, using the TIP3P water model[53] requiring a minimum distance of 12 Å between the solute and the box border. The total number of water molecules was 18605 (Apo M^{pro}), 23453 (Apo PL^{pro}), 18555 [$(PhSe)_2 + M^{pro}$], and 29325 [$(PhSe)_2 + PL^{pro}$]. The simulated systems have a total number of atoms equal to 60504 (Apo M^{pro}), 75257 (Apo PL^{pro}), 60378 [$(PhSe)_2 + M^{pro}$], and 92899 [$(PhSe)_2 + PL^{pro}$]. A NaCl concentration of 0.15 M was used, with four Na^+ ions added to neutralize the net charge of the M^{pro} complex; no addition of extra ions was necessary to neutralize the PL^{pro} complex.

The systems' initial gradient minimization stage was completed in two rounds. A strong harmonic constraint of 100 kcal mol^{-1} Å^2 was applied to the solute atoms in the first round of minimization, and 6,000 steps of minimization (1000 steps of steepest descent minimization + 5000 steps of conjugate gradient minimization) were performed. The second minimization consisted of 4000 steps with no constraints (1000 steps of steepest descent minimization + 3000 steps of conjugate gradient minimization).

After the minimization, each system was gradually heated to 298 K over 50 ps. Finally, a 50 ns simulation under isothermal–isobaric (*NPT*) conditions was performed before proceeding to production simulation. After a 50 ns equilibration (Figure S5 in the Supporting Information), the system was subjected to a 200 ns simulation for $(PhSe)_2 + M^{pro}$, a 200 ns simulation for the Apo M^{pro} structure, a 100 ns simulation for $PL^{pro} + (PhSe)_2$, and a 100 ns simulation for Apo PL^{pro} using a 2 fs integration time step. Throughout the simulation, the temperature was controlled by a Langevin thermostat,[54] and the pressure was maintained at 1 bar by a Berendsen barostat.[55] During the production runs, coordinates were saved every 20 ps, yielding a total of 10,000 structures for a 200 ns long MD trajectory. The trajectories were visualized

using VMD 1.9.363[56] and Discovery Studio.[57] The trajectories of the $(PhSe)_2 + M^{pro}/PL^{pro}$ systems were analyzed through CPPTRAJ[58] to generate the root mean square deviation (RMSD) plots. The number of $(PhSe)_2 - M^{pro}$ residue contacts was determined with a threshold of 4.5 Å. Using the covariance matrix obtained from our 3D data, for a principal component analysis, the 2D projections with respect to selected eigenvector components were plotted.

The last 50 ns interval of the MD trajectories of each system was used to compute the binding free energy between $(PhSe)_2$ and M^{pro}/PL^{pro}. To this end, we initially used the molecular mechanics with generalized Born and surface area solvation (MM-GBSA) method,[59] which is commonly used for proteins.[60,61] The snapshots were sampled at 200 ps intervals, yielding a total of 251 frames for calculating the MM-GBSA energies. The binding free energy ΔG_{bind} was calculated using the MM-GBSA as follows

$$\Delta G_{bind} = \Delta E_{MM} + \Delta G_{solv} - T\Delta S \quad (1)$$

In this case, ΔE_{MM} is the sum of non-bonded and bonded interaction energies.[62] ΔG_{solv} is the sum of the polar and non-polar solvation contributions, where the polar terms are calculated using a generalized Born model solver and the non-polar terms are computed based on the size of the solvent-accessible surface area in $(PhSe)_2$ and M^{pro}/PL^{pro}. The last term, which corresponds to conformational entropy $T\Delta S$, is computationally expensive, and previous studies[63,64] demonstrated that including the entropic contribution in the ΔG_{bind} calculations does not guarantee a better agreement of the calculated binding free energy with experimental data due to the inherent approximate nature of the calculation of the entropic term. All MM-GBSA calculations in this study were performed with the AmberTools-20[58] MMPBSA.py script.[65] The per residue decomposition analyses (idecomp = 1) using the MD trajectories were also performed to identify the key $(PhSe)_2$−residue energetic contributors to the binding free energy.[66]

In order to better quantify the binding energy in the case of the M^{pro} system, we calculated the binding energy also with molecular mechanics Poisson−Boltzmann surface area (MM-PBSA) which is an analogous method to estimate ligand binding affinities and is implemented in AmberTools-20 software.

2.2.3. DFT Calculations. Two enzymatic clusters were extracted from the MD simulations. In both cases, the M^{pro} residues within a cutoff of 4.0 Å from $(PhSe)_2$, i.e., H41, M49, C145, and M165, were chosen and removed from the catalytic pocket; the CH_3CO and CH_3NH groups were added to the N- and C-terminal regions, respectively, to mimic the backbone peptide bonds. The total number of atoms was 134. Gaussian16[67] was used to perform all DFT calculations. The B3LYP hybrid functional[68,69] was employed and combined with the Grimme D3 dispersion correction and the Becke−Johnson damping function.[70,71] The 6-311G(d,p) basis set was used to describe all first and second period atoms, while Dunning's correlation-consistent cc-pVTZ basis set was used to describe sulfur and selenium atoms. All structures were optimized in the gas phase and in a solvent (water) using the SMD solvation model[72] [level of theory: (SMD-)B3LYP-D3(BJ)/6-311G(d,p), cc-pVTZ] keeping frozen the backbone atoms (see Tables S11−S13 in the Supporting Information for a complete list of the frozen atoms). Solvent effects were included using a continuum model as done also in previous

studies on enzymatic clusters.[73−75] Thermodynamic corrections were calculated using standard statistical mechanics relations based on electronic energies and gas phase frequency calculations at 298.15 K and 1 atm, as implemented in Gaussian software. All energies described in the main text are relative Gibbs free (ΔG) energies. To assess the nature of the optimized geometries, frequency calculations were performed: each transition state has one imaginary frequency that is related to the normal mode connecting the preceding and the following intermediate. All minima have no imaginary frequencies. For validation purposes, starting from the transition states, an intrinsic reaction coordinate (IRC) calculation was performed, to ensure that the proper transition state was located.

3. RESULTS AND DISCUSSION

3.1. Experimental Results. To assess the efficacy of $(PhSe)_2$ in SARS-CoV-2 replication inhibition, we performed *in vitro* assays using the Vero E6 model of cells. Cells infected with SARS-CoV-2 were treated with different concentrations of $(PhSe)_2$ (Figure 1). The EC_{50} and CC_{50} values are shown in
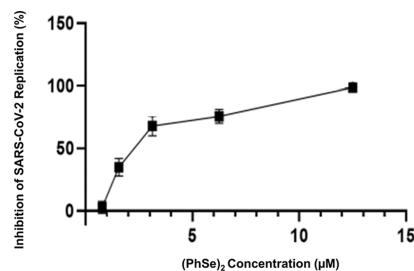

Figure 1. $(PhSe)_2$ inhibits SARS-CoV-2 replication in Vero E6 infected cells. Data points are expressed as mean ± SEM, and when the error is not visible, the bars are hidden by the symbols.

Table 1. We analyzed the cell toxicity by MTT assay. The CC_{50} for Vero E6 cells was about 25 μM, and the EC_{50} for SARS-CoV-2 in this cell model was 2.4 μM. The EC_{50} value is comparable to that of observed FDA-approved drugs repurposed for the treatment of COVID-19 during 2020.[76] Moreover, the $(PhSe)_2$ EC_{50} is lower than that of other M^{pro} inhibitors, including ebselen.[77,78] In addition, it is important to highlight that the beneficial effect of organoselenium compounds is not restricted only for inhibition of virus replication but also has potential beneficial effects in COVID-19 with a number of targets critical to pathogenesis, such as attenuation of inflammatory oxidants and cytokines, as already observed for ebselen, being interesting to also be evaluated for $(PhSe)_2$.[23,27−29,31,78]

3.2. Non-Covalent $(PhSe)_2 + M^{pro}/PL^{pro}$ Systems. The MD simulations shed light on the dynamic evolution in water of both M^{pro} and PL^{pro} in the presence of the ligand. Upon analyzing the MD trajectories of the $(PhSe)_2 + M^{pro}$ and $(PhSe)_2 + PL^{pro}$ systems (details are in Materials and Methods Section 2.2.2), analogies among the $(PhSe)_2$ interactions with the proteases were observed: (i) stacking of the $(PhSe)_2$ phenyl rings with H41 in M^{pro} and H272 in PL^{pro} and (ii) hydrophobic interactions of the rings with M49 and M165 in M^{pro} and W106, Y112, Y264, Y268, and L162 in PL^{pro}.

Using a distance threshold of 4.5 Å, a total of 38,132 contacts with $(PhSe)_2$ were recorded throughout the simulation of $(PhSe)_2 + M^{pro}$ (Figure 2A). T25 accounts for
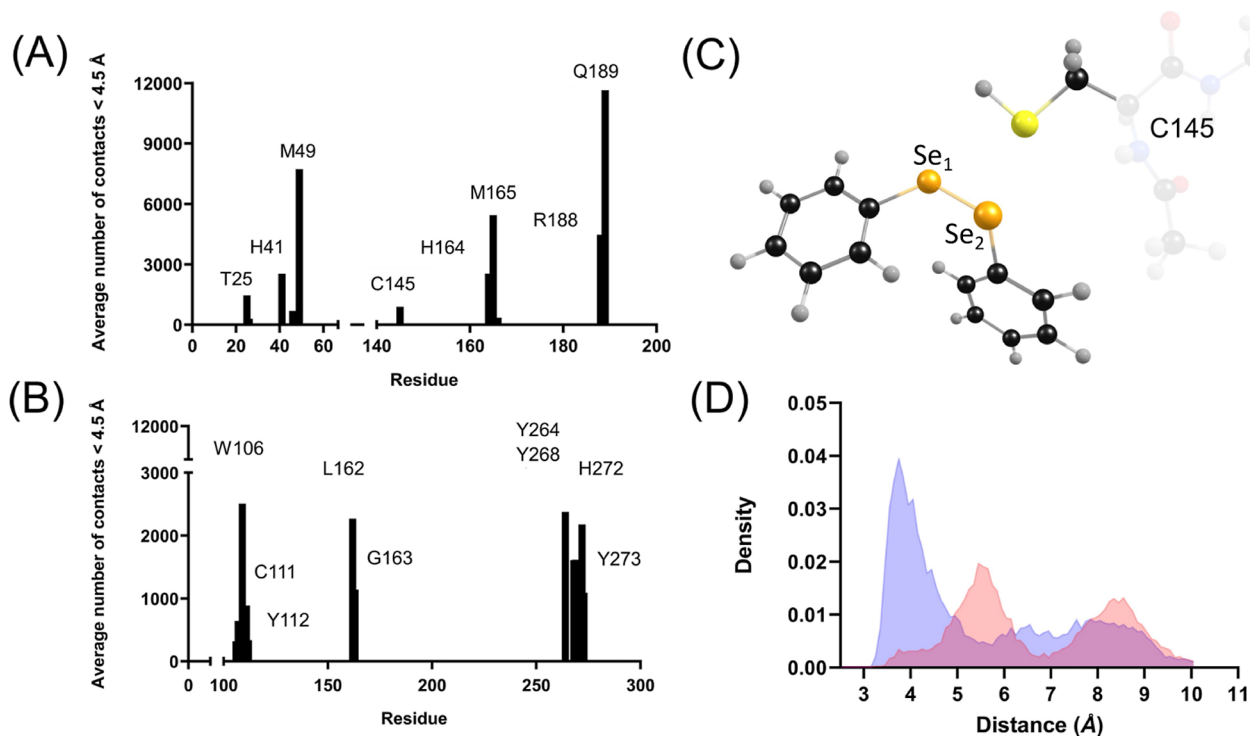
Figure 2. Average number of contacts between $(PhSe)_2$ and (A) SARS-CoV-2 M^{pro} and (B) PL^{pro}. Cut-off distance: 4.5 Å. (C) Structural details of $(PhSe)_2$ in the active site of M^{pro}, showing the mutual arrangement of Se atoms (Se_1 and Se_2) and S of C145. (D) Probability densities in M^{pro} of the distances between C145−S and Se_1 of $(PhSe)_2$, in blue, and Se_2 of $(PhSe)_2$, in red. The probability densities were obtained using the radial distribution function, which is the probability of finding a pair of atoms a distance r apart relative to the probability for a completely uniform distribution.
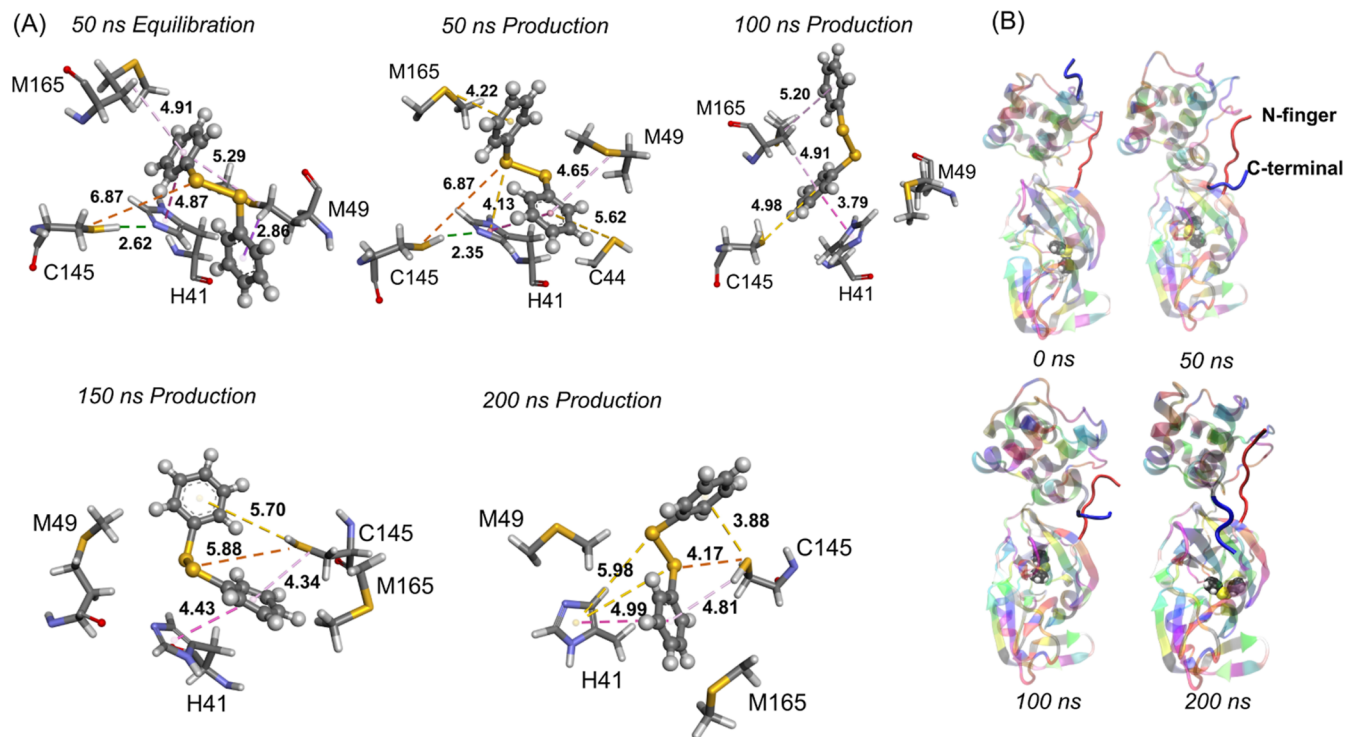
Figure 3. (A) $(PhSe)_2$ + M^{pro} snapshots taken at different times during the simulation. The Se−S distance is represented in brown; the $\pi-\pi$ stacking interaction is represented in pink; π−sulfur interaction with M49, M165, C44, and C145 is shown in gold and the C145-Sγ to Nε atom of H41 in green. (B) N-terminal (red) and C-terminal (blue) of the $(PhSe)_2$ + M^{pro} system.

approximately 4% of total contacts, M165 accounts for approximately 14% of total contacts, M49 accounts for

approximately 20% of total contacts, and Q189 accounts for approximately 31% of total contacts. The two dyad residues,
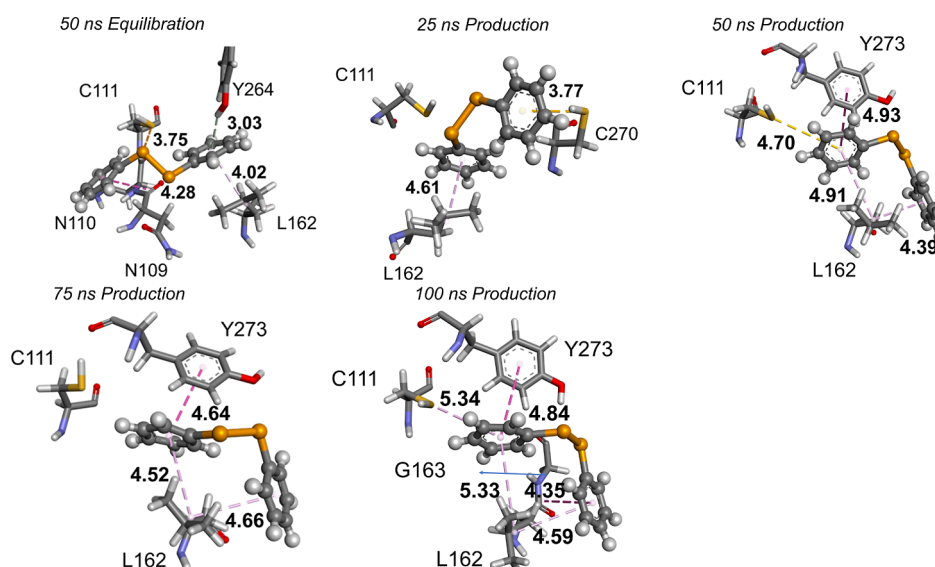
Figure 4. $(PhSe)_2$ + PL^{pro} snapshots. The S–Se distance is represented in brown; the π–π stacking interaction is represented in pink; π–sulfur interaction with C111 is shown in gold.
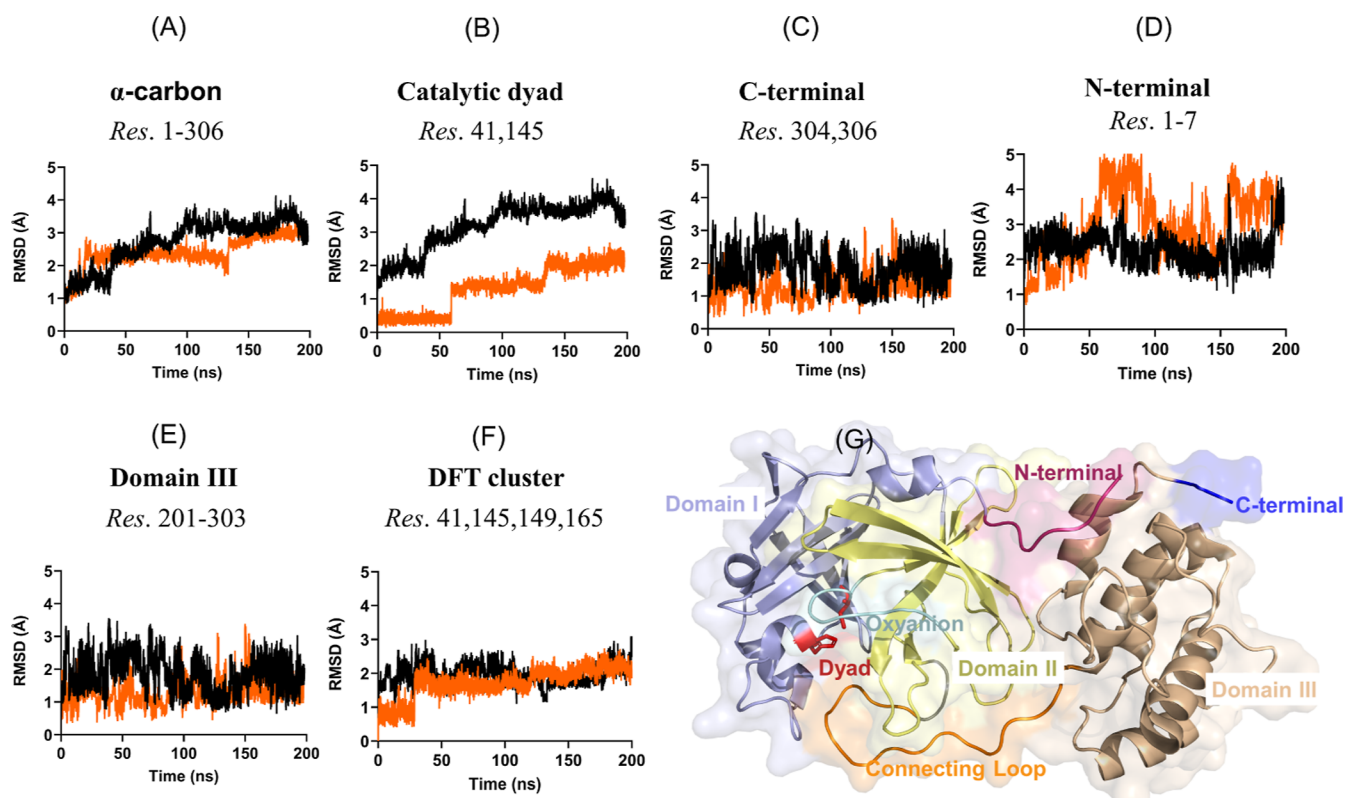

Figure 5. RMSD plots of the (A) α-carbon backbone, (B) catalytic dyad, (C) C-terminal, (D) N-terminal, (E) domain III, and (F) residues used to extract the DFT cluster (vide infra). The average RMSD of $(PhSe)_2$ + M^{pro} is represented in orange and the Apo structure in black. (G) The catalytic dyad is colored red, the N-terminal magenta, the C-terminal blue, domain I light blue, domain II pale-yellow, domain III wheat, the oxyanion loop cyan, and the connecting loop orange.

H41 and C145, account for about 9% of the total contacts. In $(PhSe)_2$ + M^{pro}, contacts with the conserved residues are continuously maintained, thus establishing a favorable binding region for $(PhSe)_2$ in the M^{pro} binding site.

In PL^{pro} (Figure 2B), $(PhSe)_2$ maintains contacts with the triad's C111, H272, and D286 residues. The distance of D286 from $(PhSe)_2$ exceeds 4.5 Å, and it acts as a stabilizer for the H272 proton exchange function in catalysis. Apart from the

triad's residues, $(PhSe)_2$ makes several contacts with W106, Y112, L162, G163, Y264, Y268, and Y273 at less than 4.5 Å.

In terms of proximity to the S atom of C145, $(PhSe)_2$ poses in the active site of SARS-CoV-2 M^{pro} remain very similar to the starting docking pose and differ only in their stacking conformation during the MD simulations. The S atom of C145 remains close to both Se atoms of $(PhSe)_2$ (Figure 2C,D). According to the distributions shown in Figure 2D, the most

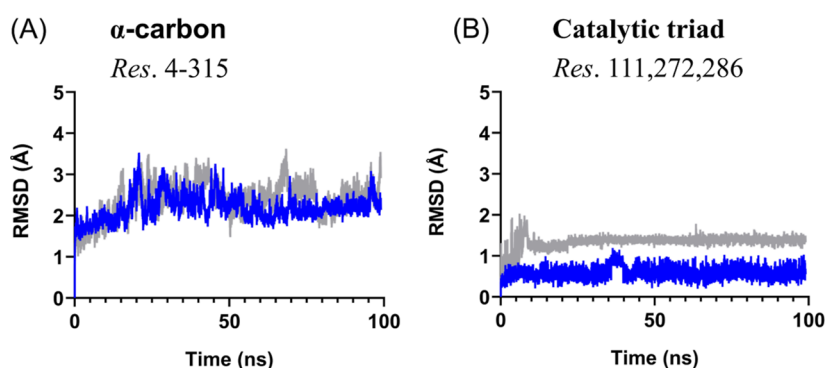**Figure 6.** RMSD plots of the (A) backbone and (B) catalytic triad. The average RMSD of $(PhSe)_2 + PL^{pro}$ is represented in blue and the Apo structure in gray.

probable values of the distances $S-Se_1$ are 3.7 Å and $S-Se_2$ are 5.4 Å. The larger distances observed in the second peak are configurations that correspond to a conformational change of the side chain of C145 from trans to gauche to accommodate the stabilizing H41 π-stacking interaction (Figure 3A). Snapshots taken at different times during the simulation are shown in Figure 3. The analysis of RMSD of the protein with the ligand shows that this system configuration is stable over time (200 ns) (see the next section). In $(PhSe)_2 + M^{pro}$, the catalytic dyad remains hydrogen-bonded with the thiol proton pointing toward the $N\varepsilon$ atom of H41 up to 50 ns of simulation time before C145 assumes gauche conformation.

On the C-terminal of both the $(PhSe)_2 + M^{pro}$ system and the Apo (or ligand-free) structure, which has been simulated too, a significant conformational change is observed during the simulation. This can be observed in Figure 3B, where the original direction of the C-terminal at 0 ns is maintained until about 30 ns; then, it flips to a conformation which is conserved for the rest of the simulation. This latter appears to be the stable conformation of the protease (Figure 3B). Upon analyzing the interaction of the diselenide with the closest residues, it is seen that M49, M165, and Q189 interact via hydrophobic, $\pi-$alkyl, and $\pi-$sulfur interactions. Y54 favors a $\pi-\pi$ stacking interaction (4.13 Å at 75 ns) in combination with the $\pi-$sulfur interaction involving C44. $(PhSe)_2$ conformation changes continuously, but one of its phenyl rings remains in a $\pi-\pi$ stacking position with H41.

Considering $(PhSe)_2 + PL^{pro}$ at 50 ns, i.e., at the end of the equilibration, the protease has several $\pi-$alkyl and $\pi-$hydrogen interactions with one of the phenyl rings of the diselenide (Figure 4). These interactions change over time to more stabilizing $\pi-$stacking interactions with Y273. In addition, the phenyl rings of $(PhSe)_2$ are involved in $\pi-$interactions with the propyl group of the L162 side chain. Due to their mobility, the phenyl rings also establish interactions with N109, N110, C111, G163, and C270.

We found evidence that the ligand well fits in both proteases and remains close to the catalytic key residues, without any constraint. Its non-covalent inhibitory capacity was further explored by quantifying the stability of the systems and the interaction energies, as described in the next sections.

3.2.1. Stability of $(PhSe)_2 + M^{pro}/PL^{pro}$ Systems during MD Simulations. The stability of the $(PhSe)_2 + M^{pro}$ non-covalent system was analyzed referring to fluctuations of different regions (see Figures 5 and S3 in the Supporting Information). As shown in Figure 5A, the α-carbon RMSD plots of the Apo and the $(PhSe)_2 + M^{pro}$ system show the effect of the ligand

binding on the protein dynamics. The average backbone RMSD variation of $(PhSe)_2 + M^{pro}$ is in the range 1.0−2.9 Å, when compared to that in the range 1.0−3.5 Å for the Apo M^{pro} structure, clearly suggesting that the binding of the diselenide has only a limited impact on the structural dynamics of the enzyme. Then, we analyzed the stability of $(PhSe)_2$ in the C145−H41 catalytic binding site, which exhibits an average RMSD in the range of 0.2−2.1 Å (Figure 5B). These low RMSD values, i.e., <3 Å, indicate that $(PhSe)_2$ dynamics does not affect the compactness of the catalytic site, which was further ascertained by computing the average radius of gyration (R_g) resulting in 22.3 Å for the Apo structure and 22.2 Å for $(PhSe)_2 + M^{pro}$ (Figure S2). These results indicate that the influence of $(PhSe)_2$ binding on the overall M^{pro} structure is negligible. Small RMSD fluctuations are observed also in the oxyanion loop (Figure S3B in the Supporting Information) and in the long loop connecting domains II and III (Figure S3A in the Supporting Information) and C and N-terminals (Figure 5C,D). We found that domains I and II remain quite stable throughout the simulation with backbone RMSD changes being within ∼0.5−0.9 Å (Figure S3C,D in the Supporting Information). Conversely, domain III, which features five helices, exhibits higher fluctuations exceeding 3.0 Å (Figure 5E). These findings are fully consistent with previous stability reported behavior for ligand + M^{pro} systems.[48,79] Finally, we also analyzed the changes displayed by the residues that compose the active site and used them in the cluster for the DFT calculations to model the covalent inhibition mechanism (vide infra). Both the Apo and the M^{pro}-$(PhSe)_2$ complex showed very similar stable rmsds at approximately 2 Å, a sign that the active site does not undergo strong modification during the simulation, and the presence of $(PhSe)_2$ does not drastically change the active site conformation.

Also, the conformational changes of $(PhSe)_2 + PL^{pro}$ and Apo PL^{pro} were evaluated using the RMSD analysis (Figure 6). The two systems show an average RMSD of 2.20 Å for the $(PhSe)_2 + PL^{pro}$ and of 2.40 Å for the Apo PL^{pro} structure. The compactness of the two systems is also similar, as illustrated by R_g (Figure S2B). The modest impact of the binding of $(PhSe)_2$ to PL^{pro} can be appreciated in the triad's stability when compared to Apo PL^{pro} with 1 Å change in the RMSD.

When comparing principal component (PC) projections between different MD simulations, we obtain a criterion of similarity between the dominant modes of motion sampled along the different trajectories. PCA is performed in such a way that PC1 (the first principal component) exhibits the greatest
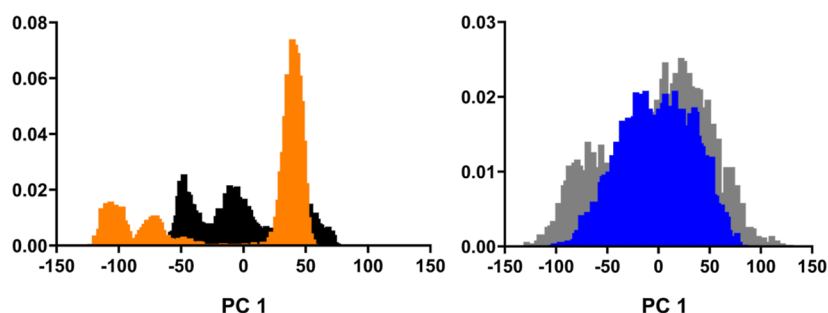
Figure 7. Overlap of principal component 1 (PC1) histograms from PCA in Cartesian space. (A) $(PhSe)_2$ + M^{pro} (orange) and Apo M^{pro} (black). (B) $(PhSe)_2$ + PL^{pro} (blue) and Apo PL^{pro} (gray).
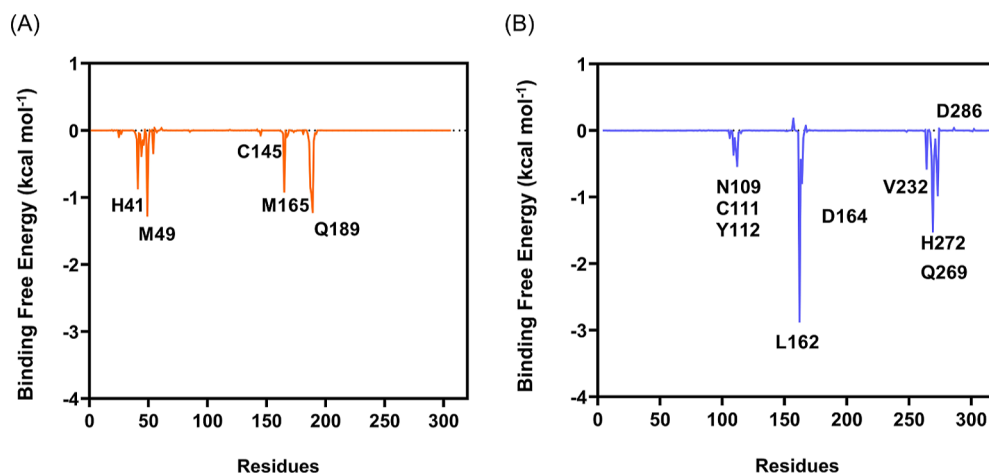

Figure 8. Binding free energy (kcal mol^{-1}) decomposition per residue, for (A) $(PhSe)_2$ + M^{pro} (orange) and (B) $(PhSe)_2$ + PL^{pro} (blue).

variance in the sampled motion. We performed PCA on the trajectories of both $(PhSe)_2$ + protease and Apo protease. Figure 7 shows the overlap of histograms of PC 1 projections for the simulations.

The simulations for $(PhSe)_2$ + M^{pro} and Apo M^{pro} have different distributions for PC1, but the number of modes is conserved, indicating that these motions are not disruptive, which is consistent with the observations of the RMSD plots (Figure 5A). Conversely, the simulations of $(PhSe)_2$ + PL^{pro} and Apo PL^{pro} have significant overlap, suggesting that similar dynamic modes were sampled.

Based on the equilibrium trajectories, MM-GBSA calculations were carried out to explore the binding affinity between $(PhSe)_2$ and M^{pro} (Table S5)/PL^{pro} (Table S6). The binding free energy of $(PhSe)_2$ to M^{pro} is -19 kcal mol^{-1}; in the case of PL^{pro}, it is -23 kcal mol^{-1}. These values indicate a neatly favorable stabilizing role of both catalytic pockets toward this ligand. To identify the M^{pro}/PL^{pro} residues involved in the $(PhSe)_2$ binding, the computed free energies were decomposed into single residue contributions.

The energy decomposition (Figure 8) indicates that the four conserved residues (H41, M49, M165, and Q189) are those that mostly contribute to the binding of $(PhSe)_2$ and M^{pro}. Regarding PL^{pro}, L162, D164, Q269, and H272 are the four residues providing the highest contributions to the binding energy, mainly via hydrophobic and alkyl$-\pi$ interactions (L162) and π-stacking (H272); the whole decomposition is provided in the Supporting Information (Tables S7 and S8).

Binding energies obtained with the MM-PBSA approach were calculated for M^{pro} with results showing a binding energy

of -5 kcal mol^{-1} for the last 50 ns of the trajectory. To ensure the accuracy of this result, we also computed the binding affinity using the whole production trajectory of 200 ns (for a total of 1000 snapshots). Results showed a slightly more favorable binding activity of -8 kcal mol^{-1} (the full decomposition of the binding energies can be found in Supporting Information, Tables S9 and S10) which confirms the favorable ligand–protein binding in M^{pro}.

3.2.2. Torsional Motions of $(PhSe)_2$ in M^{pro} and PL^{pro}. It is well known that the phenyl rings of $(PhSe)_2$ freely rotate in solution.[51,80,81] This motion can be followed by measuring the values of the dihedrals θ_1 and θ_2 (Figure 9). Conversely, the value of the main dihedral Ψ is close to 90 or $-90°$, characterizing two conformations which easily interconvert at room temperature. An accurate computational analysis showed that $(PhSe)_2$ has two minimum energy structures corresponding to two distinct mutual orientations of the phenyl rings, denoted closed and open conformations[51,75,80] (Figure 9).

This conformational behavior was observed also in the catalytic pockets of M^{pro} and PL^{pro} during the MD simulations. The dihedral angle Ψ and the dihedrals θ_1 and θ_2 were examined during the 200 ns simulation time. The Ψ distributions in M^{pro} and PL^{pro} closely resemble the results of free $(PhSe)_2$ in water, with peaks close to $\pm 90°$,[51] although in protein, they are not perfectly symmetric, and the peak intensities are not equivalent (Figure 10) due to specific interactions with the surrounding residues.

During the simulations, in M^{pro} and PL^{pro}, the Se–Se bond length is well maintained, with average values of 2.37 and 2.28 Å, respectively. The same is true for the C–Se/C′–Se′ bonds
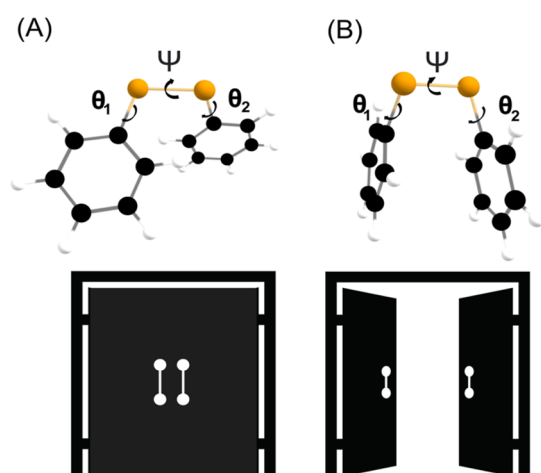
Journal of Chemical Information and Modeling
pubs.acs.org/jcim
Article

Figure 9. (A) Closed and (B) open conformations of $(PhSe)_2$ with the main dihedral angles C−Se−Se−C (Ψ) and C−C−Se−Se (θ_1 and θ_2).

and C−Se−Se′/C′−Se′−Se angles, which have average values of 1.97 Å and 103° for $(PhSe)_2$ in M^{pro} and 1.95 Å and 107° for $(PhSe)_2$ in PL^{pro}, respectively. Regarding the orientation of the phenyl rings of $(PhSe)_2$, in both proteases, the distributions are similar, with the closed conformer being more easily found (peaks at 0 and 180°, Figure 11). These findings are consistent with Torsello's results[51] and with experimental findings[82] in solution.

The dynamics of $(PhSe)_2$ characterized by flip-flop and rotation of the phenyl rings is nicely maintained in protein, suggesting that also in the complex anisotropic environment, the conformational barriers are modest.[83] The dominant Ψ dihedral conformation at +90° and at θ_1 and θ_2 values of 0°/ 180° for diphenyl diselenide in M^{pro} was chosen for the DFT mechanistic investigation on the M^{pro} cluster.

3.3. M^{pro} Covalent Inhibition by $(PhSe)_2$. The mechanism of covalent inhibition of these proteases by $(PhSe)_2$ implies the formation of a S−Se bond with cleavage of the Se−Se bond of the ligand. Deprotonation of the catalytic cysteine is mandatory since it activates the nucleophilic potential of the chalcogen, and in both cases, proton transfer from Cys to His may be postulated. As described above, the RMSD of $(PhSe)_2$ + M^{pro} shows a very stable dyad with minimal fluctuations and an average value of 1.0 Å, whereas in the absence of $(PhSe)_2$, as in the case of the Apo, the average RMSD increases to 3.0 Å (Figure 5B). The stability of $(PhSe)_2$ + M^{pro} limits the conformational freedom of C145 and H41 residues. Similar stable behavior is seen in the PL^{pro} catalytic triad (C111, H272, and D286) (Figure 6B) with a lower

average RMSD of 0.57 Å, much lower than the RMSD of the triad of the Apo structure (1.34 Å). Analysis of the contacts reveals that $(PhSe)_2$ remains in the catalytic pocket of M^{pro} and of PL^{pro}.

In Scheme 1C,D, our proposed mechanism of activated nucleophilic C sulfur attacking selenium in the diselenide ligand to form an inhibited product (PInhb) is shown. Due to this close analogy, we have focused on the mechanistic details of covalent inhibition using a cluster extracted from $(PhSe)_2$ + M^{pro}. In order to probe the effect of different conformations of the residues and of the arrangement of $(PhSe)_2$ within the catalytic pocket on the reaction, two different enzymatic clusters were extracted from the MD simulations. A cluster was extracted at 46.2 ns with a Ψ value of −91° and a S−Se−Se angle amplitude of ≈80°. For the mechanistic study, all key residues C145, H41, M165, and M49, except Q189 [distance from $(PhSe)_2 > 4.0$ Å], were included in a cluster which was treated at (SMD-)B3LYP-D3(BJ)/6-311G(d,p),ccPVTZ. The coordinates of the second reactant complex (RC) were extracted from an equilibrated 88 ns MD snapshot which has the dominant Ψ at +94° and C145-Sγ to the Nε atom of H41 at 2.16 and 4.30 Å to the selenium atom of $(PhSe)_2$. Importantly, all the included residues are conserved residues and are found within 4 Å from $(PhSe)_2$ and have been all verified by the contact analysis and MD energy decomposition to play important roles in the binding of $(PhSe)_2$. The backbone atoms of the catalytic pocket were constrained to maintain the conformation found in the protein environment as obtained from the MD simulations at the corresponding times (the full list of constrained atoms in the cluster can be found in the Supporting Information). Capping groups were used to saturate terminal residues mimicking a peptide bond. At the N-terminus, an acetyl group was linked, and at the C-terminus, an amide group was connected (Figure 12). Poses at later times were not investigated due to a change of position of the $(PhSe)_2$ molecule at about 100 ns (see movie in the Supporting Information) which makes the proposed mechanism unfeasible due to the phenyl rings of the ligand being found between Cys145 and His41, making the initial proton transfer difficult to model (vide infra).

For both clusters, similar mechanistic features were investigated, and the energetics of the two inhibition mechanisms were comparable. Thus, only results obtained starting from the snapshot at 46.2 ns will be discussed. Results obtained starting from the snapshot at 88 ns can be found in the Supporting Information. The probed inhibitory mechanism closely resembles the acylation phase of the fully functional M^{pro} described in Scheme 1A. The presence of $(PhSe)_2$ does not prevent C145 activation, which is deprotonated by H41 with an activation energy of 5.28 kcal mol^{-1}; a zwitterionic
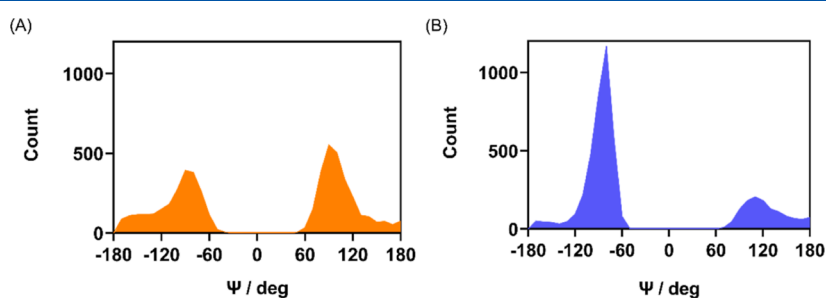

Figure 10. Distributions of the dihedral Ψ in the catalytic pocket of (A) M^{pro} and (B) PL^{pro}.
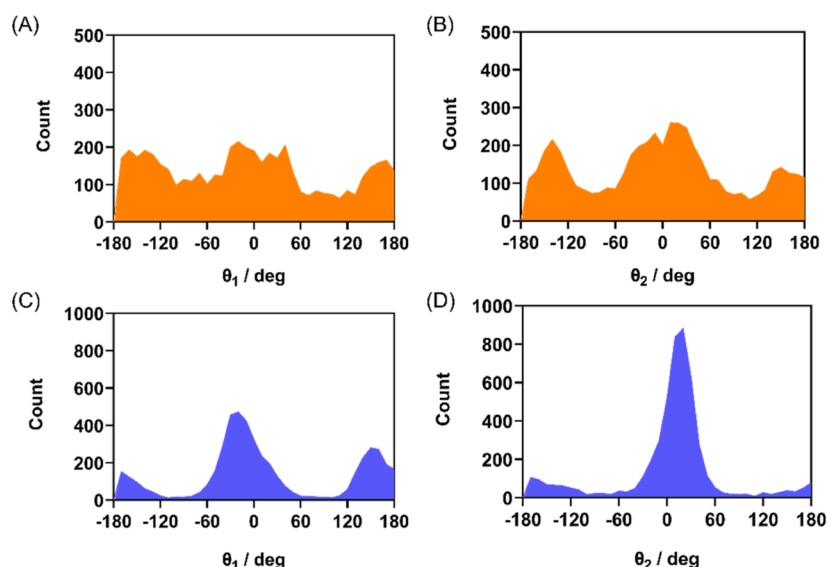
Figure 11. Distributions of the dihedrals θ_1 and θ_2 in (A) and (B) M^{pro} and (C) and (D) PL^{pro}.
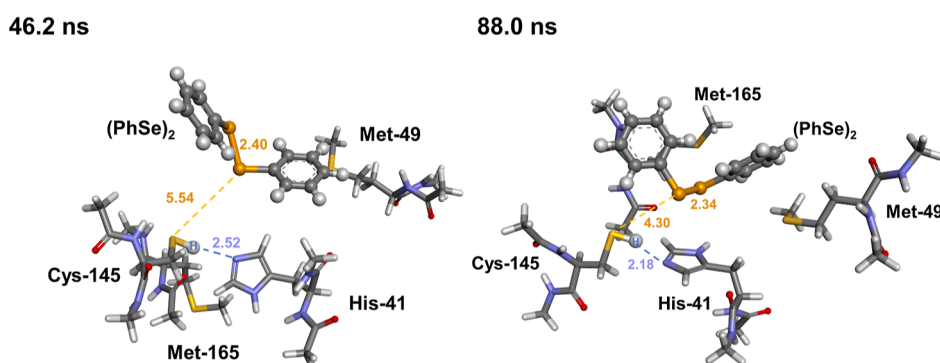

Figure 12. Optimized catalytic clusters (RC) for the mechanistic investigation of covalent M^{pro} inhibition by $(PhSe)_2$, taken from MD snapshots at 46.2 ns (left) and at 88 ns (right). Level of theory: SMD(Water)-B3LYP-D3(BJ)/6-311G(d,p),ccPVTZ.

intermediate formed by deprotonated cysteine (C) and protonated histidine (HIP) was found on the potential energy surface (PES) at 6.33 kcal mol^{-1} above the initial RC. This point is higher than the transition state leading to it on the Gibbs free energy surface, but it is correctly located at slightly lower energy on the electronic energy surface. This is thus considered an artifact of the thermodynamic correction and is common in those cases in which the transition state and the zwitterion are close in energy on the electronic PES. After proton transfer from C145 to H41, the activated cysteinate residue attacks the weak electrophilic Se atom of $(PhSe)_2$, resulting in a three-center intermediate (TCI) with an almost linear S−Se−Se arrangement of the 2.46 Å C(S)−Se bond and 2.81 Å Se−Se $(PhSe)_2$ bond. This step occurs without an appreciable activation energy, only requiring a slight conformational rearrangement of $(PhSe)_2$ within the catalytic pocket. The TCI is located at 1.71 kcal mol^{-1} above the initial RC, and the overall step is thus weakly endergonic. Further breaking of the Se−Se bond was found to occur also without an appreciable activation energy, leading to a free selenolate and to fully formed S−Se bonds. This adduct (PInhb) lies at −0.95 kcal mol^{-1} with respect to the initial RC, and the overall inhibition process is thus very weakly exergonic/isoergonic. Further protonation of PhSe$^-$ via back-proton transfer from HIP leads to higher-energy products (product complex, PC),

located at 3.75 kcal mol^{-1} above the RC. Thus, no attempt to locate the transition state for such a process was pursued. For the snapshot at 88 ns, the transition state for this process was associated with high activation energy (10.7 kcal mol^{-1}, Figure S4), further suggesting that this process likely does not occur.

The energetics here provided does not suggest a strong covalent inhibition, with the overall process being only very weakly favored from the thermodynamic point of view. However, at least partly, $(PhSe)_2$ is expected to bind to Cys145. The energetics can still be safely compared to the one computed for the covalent binding of ebselen to M^{pro} provided by some of us.[6] For this latter organoselenium compound, the inhibited product was located at ca. −7 kcal mol^{-1} with respect to the RC. Thus, our calculations predict a lower (covalent) inhibition strength of $(PhSe)_2$ compared to ebselen, in nice agreement with the experimental findings.

4. CONCLUSIONS

In this work, starting from the *in vitro* effects of $(PhSe)_2$ on SARS-CoV-2 replication, using Vero E6 cells, we investigated one of the possible molecular aspects of inhibition using MD simulations and quantum mechanics (DFT) calculations. Experimental findings show an inhibitory concentration in the low micromolar range. The adduct between M^{pro}/PL^{pro} and $(PhSe)_2$ is stable in the simulation time, with $(PhSe)_2$

phenyl rings buried between histidine residues and residues Met165, Met49, and Cys145 via π-stacking interactions between the imidazole ring of histidine and the phenyl ring of $(PhSe)_2$, as confirmed by examining the key dihedral angle Ψ (C−Se−Se−C′) and supporting dihedrals θ1 and θ2 of $(PhSe)_2$. From the mechanistic point of view, we found that the covalent S−Se bond formation is only slightly energetically favored, in agreement with the fact that $(PhSe)_2$ appears to be a less effective covalent inhibitor than the well-known ebselen, for which a thermodynamically favored S−Se bond formation was previously reported.[6,13]

Further computational and experimental work is required to design $(PhSe)_2$ derivatives and new molecules with organo-diselenide scaffolds as inhibitors of viral proteases, offering an appealing strategy for combating SARS-CoV-2.

■ ASSOCIATED CONTENT

ⓈⒾ Supporting Information

The Supporting Information is available free of charge at https://pubs.acs.org/doi/10.1021/acs.jcim.3c00168.

> Force field parameters for $(PhSe)_2$, PES scans [B3LYP/6-311G(d,p),ccPVTZ], radius of gyration plots, RMDS plots, equilibration plots, MM/GBSA energy results, total MM/GBSA and MM/PBSA energy decomposition results, reaction energies [SMD-B3LYP-D3(BJ)/6-311G(d,p),ccPVTZ] for $(PhSe)_2$ + Cys in the neutral and anionic form, and coordinates of the QM structures (PDF).

■ AUTHOR INFORMATION

Corresponding Authors

Milene Dias Miranda − *Laboratório de Vírus Respiratórios e Do Sarampo, Instituto Oswaldo Cruz and Laboratório de Morfologia e Morfogênese Viral, Instituto Oswaldo Cruz, Fundação Oswaldo Cruz, Manguinhos, Rio de Janeiro 21041-210, Brazil;* ⓞ orcid.org/0000-0003-0037-059X; Email: mmiranda@ioc.fiocruz.br

Laura Orian − *Dipartimento di Scienze Chimiche, Università Degli Studi di Padova, Padova 35131, Italy;* ⓞ orcid.org/0000-0002-1673-5111; Email: laura.orian@unipd.it

Authors

Folorunsho Bright Omage − *Departamento de Bioquímica e Biologia Molecular, Universidade Federal de Santa Maria, Santa Maria, Rio Grande do Sul 97105-900, Brazil;* ⓞ orcid.org/0000-0002-9750-5034

Andrea Madabeni − *Dipartimento di Scienze Chimiche, Università Degli Studi di Padova, Padova 35131, Italy;* ⓞ orcid.org/0000-0002-0407-0263

Amanda Resende Tucci − *Laboratório de Vírus Respiratórios e Do Sarampo, Instituto Oswaldo Cruz and Laboratório de Morfologia e Morfogênese Viral, Instituto Oswaldo Cruz, Fundação Oswaldo Cruz, Manguinhos, Rio de Janeiro 21041-210, Brazil;* ⓞ orcid.org/0000-0001-8474-2973

Pablo Andrei Nogara − *Departamento de Bioquímica e Biologia Molecular, Universidade Federal de Santa Maria, Santa Maria, Rio Grande do Sul 97105-900, Brazil;* ⓞ orcid.org/0000-0002-9133-6102

Marco Bortoli − *Institute of Computational Chemistry and Catalysis (IQCC) and Department of Chemistry, Faculty of Sciences, University of Girona, Girona 17003, Spain;* ⓞ orcid.org/0000-0001-5506-6347

Alice dos Santos Rosa − *Laboratório de Vírus Respiratórios e Do Sarampo, Instituto Oswaldo Cruz and Laboratório de Morfologia e Morfogênese Viral, Instituto Oswaldo Cruz, Fundação Oswaldo Cruz, Manguinhos, Rio de Janeiro 21041-210, Brazil;* ⓞ orcid.org/0000-0002-1350-1301

Vivian Neuza dos Santos Ferreira − *Laboratório de Vírus Respiratórios e Do Sarampo, Instituto Oswaldo Cruz and Laboratório de Morfologia e Morfogênese Viral, Instituto Oswaldo Cruz, Fundação Oswaldo Cruz, Manguinhos, Rio de Janeiro 21041-210, Brazil;* ⓞ orcid.org/0000-0003-1712-2672

João Batista Teixeira Rocha − *Departamento de Bioquímica e Biologia Molecular, Universidade Federal de Santa Maria, Santa Maria, Rio Grande do Sul 97105-900, Brazil;* ⓞ orcid.org/0000-0003-3829-0595

Complete contact information is available at:
https://pubs.acs.org/10.1021/acs.jcim.3c00168

Notes

The authors declare no competing financial interest.
AMBER 2020 software [the Amber molecular dynamics Package (ambermd.org)] was used to perform mocular dynamics simulations; analyses were carried out with CPPTRAJ, a free open-source tool included in AmberTools 20. The DFT calculations were performed using Gaussian 16 Rev. A.03 (Gaussian 16|Gaussian.com). The protein−ligand interaction and docking analyses were performed using Discovery Studio Visualizer v21.1.0.20298, VMD for LINUX-AMD64, version 1.9.4a57 (April 27, 2022), AutoDockTools-1.5.6, and AutoDock Vina- 1.1.2, which can be downloaded for free at https://discover.3ds.com/discovery-studio-visualizer-download, http://www.ks.uiuc.edu/Research/vmd/, https://ccsb.scripps.edu/mgltools/,and https://vina.scripps.edu,respectively. The computational protocols are described in the Materials and Methods. The coordinates of all optimized structures are provided in the Supporting Information

■ REFERENCES

(1) Mengist, H. M.; Dilnessa, T.; Jin, T. Structural Basis of Potential Inhibitors Targeting SARS-CoV-2 Main Protease. *Front. Chem.* 2021, 9, 7.

(2) Jin, Z.; Du, X.; Xu, Y.; Deng, Y.; Liu, M.; Zhao, Y.; Zhang, B.; Li, X.; Zhang, L.; Peng, C.; Duan, Y.; Yu, J.; Wang, L.; Yang, K.; Liu, F.; Jiang, R.; Yang, X.; You, T.; Liu, X.; Yang, X.; Bai, F.; Liu, H.; Liu, X.; Guddat, L. W.; Xu, W.; Xiao, G.; Qin, C.; Shi, Z.; Jiang, H.; Rao, Z.; Yang, H. Structure of Mpro from SARS-CoV-2 and Discovery of Its Inhibitors. *Nature* 2020, 582, 289−293.

(3) Lee, J.; Worrall, L. J.; Vuckovic, M.; Rosell, F. I.; Gentile, F.; Ton, A. T.; Caveney, N. A.; Ban, F.; Cherkasov, A.; Paetzel, M.; Strynadka, N. C. J. Crystallographic Structure of Wild-Type SARS-CoV-2 Main Protease Acyl-Enzyme Intermediate with Physiological C-Terminal Autoprocessing Site. *Nat. Commun.* 2020, 115877.

(4) Mallapaty, S. India's Massive COVID Surge Puzzles Scientists. *Nature* 2021, 592, 667−668.

(5) Zhang, L. C.; Zhao, H. L.; Liu, J.; He, L.; Yu, R. L.; Kang, C. M. Design of SARS-CoV-2 Mpro, PLpro Dual-Target Inhibitors Based on Deep Reinforcement Learning and Virtual Screening. *Future Med. Chem.* 2022, 14, 393−405.

(6) Madabeni, A.; Nogara, P. A.; Omage, F. B.; Rocha, J. B. T.; Orian, L. Mechanistic Insight into SARS-CoV-2 Mpro Inhibition by Organoselenides: The Ebselen Case Study. *Appl. Sci.* 2021, 11, 6291.

(7) Sancineto, L.; Mangiavacchi, F.; Dąbrowska, A.; Pacuła, A.; Obieziurska-Fabisiak, M.; Scimmi, C.; Lei, Y.; Kong, J.; Zhao, Y.; dos Santos Machado, K.; Velasque Werhli, S.; Ciancaleoni, A. V.; Nascimento, G.; Kula-Pacurar, V.; Lenardão, A.; Yang, J.; Ścianowski, H.; Pyrc, J.; Santi, K.; Santi, C. Organoselenium mild electrophiles in the inhibition of Mpro and SARSCoV-2 replication. *CHEMRXIV* 2020, DOI: 10.26434/CHEMRXIV.12994250.V1.

(8) Ma, C.; Hu, Y.; Townsend, J. A.; Lagarias, P. I.; Marty, M. T.; Kolocouris, A.; Wang, J. E.; Disulfiram, C. Ebselen, Disulfiram, Carmofur, PX-12, Tideglusib, and Shikonin Are Nonspecific Promiscuous SARS-CoV-2 Main Protease Inhibitors. *ACS Pharmacol. Transl. Sci.* 2020, 3, 1265−1277.

(9) Węglarz-Tomczak, E.; Tomczak, J. M.; Giurg, M.; Burda-Grabowska, M.; Brul, S. Discovery of potent inhibitors of PLproCoV2 by screening a library of selenium-containing compounds. *bioRxiv* 2020, DOI: 10.1101/2020.05.20.107052.

(10) Węglarz-Tomczak, E.; Tomczak, J. M.; Talma, M.; Brul, S. Ebselen as a highly active inhibitor of PLProCoV2. *bioRxiv* 2020, DOI: 10.1101/2020.05.17.100768.

(11) Weglarz-Tomczak, E.; Tomczak, J. M.; Talma, M.; Burda-Grabowska, M.; Giurg, M.; Brul, S. Identification of Ebselen and Its Analogues as Potent Covalent Inhibitors of Papain-like Protease from SARS-CoV-2. *Sci. Reports* 2021, 11, 1−10.

(12) Menéndez, C. A.; Byléhn, F.; Perez-Lemus, G. R.; Alvarado, W.; de Pablo, J. J. Molecular Characterization of Ebselen Binding Activity to SARS-CoV-2 Main Protease. *Sci. Adv.* 2020, 6, 345−356.

(13) Nogara, P. A.; Omage, F. B.; Bolzan, G. R.; Delgado, C. P.; Aschner, M.; Orian, L.; Rocha, J. B. T. In Silico Studies on the Interaction Between Mpro and PLpro From SARS-CoV-2 and Ebselen, Its Metabolites and Derivatives. *Mol. Inform.* 2021, 40, 2100028.

(14) Ramos-Guzmán, C. A.; Ruiz-Pernía, J. J.; Tuñón, I. Unraveling the SARS-CoV-2 Main Protease Mechanism Using Multiscale Methods. *ACS Catal.* 2020, 10, 12544−12554.

(15) Díaz, N.; Suárez, D. Influence of Charge Configuration on Substrate Binding to SARS-CoV-2 Main Protease. *Chem. Commun.* 2021, 57, 5314−5317.

(16) Zanetti-Polzi, L.; Smith, M. D.; Chipot, C.; Gumbart, J. C.; Lynch, D. L.; Pavlova, A.; Smith, J. C.; Daidone, I. Tuning Proton Transfer Thermodynamics in SARS-CoV-2 Main Protease: Implications for Catalysis and Inhibitor Design. *J. Phys. Chem. Lett.* 2021, 12, 4195−4202.

(17) Świderek, K.; Moliner, V. Revealing the Molecular Mechanisms of Proteolysis of SARS-CoV-2 Mpro by QM/MM Computational Methods. *Chem. Sci.* 2020, 11, 10626−10630.

(18) Amporndanai, K.; Meng, X.; Shang, W.; Jin, Z.; Rogers, M.; Zhao, Y.; Rao, Z.; Liu, Z. J.; Yang, H.; Zhang, L.; O'Neill, P. M.; Samar Hasnain, S. Inhibition Mechanism of SARS-CoV-2 Main Protease by Ebselen and Its Derivatives. *Nat. Commun.* 2021, 12, 1−7.

(19) Antonopoulou, I.; Sapountzaki, E.; Rova, U.; Christakopoulos, P. Inhibition of the Main Protease of SARS-CoV-2 (Mpro) by Repurposing/Designing Drug-like Substances and Utilizing Nature's Toolbox of Bioactive Compounds. *Comput. Struct. Biotechnol. J.* 2022, 20, 1306−1344.

(20) Kneller, D. W.; Phillips, G.; O'Neill, H. M.; Jedrzejczak, R.; Stols, L.; Langan, P.; Joachimiak, A.; Coates, L.; Kovalevsky, A. Structural Plasticity of SARS-CoV-2 3CL M Pro Active Site Cavity Revealed by Room Temperature X-Ray Crystallography. *Nat. Struct. Biol.* 2003, 11, 3202.

(21) Anirudhan, V.; Lee, H.; Cheng, H.; Cooper, L.; Rong, L. Targeting SARS-CoV-2 Viral Proteases as a Therapeutic Strategy to Treat COVID-19. *J. Med. Virol.* 2021, 93, 2722−2734.

(22) Osipiuk, J.; Azizi, S. A.; Dvorkin, S.; Endres, M.; Jedrzejczak, R.; Jones, K. A.; Kang, S.; Kathayat, R. S.; Kim, Y.; Lisnyak, V. G.; Maki, S. L.; Nicolaescu, V.; Taylor, C. A.; Tesar, C.; Zhang, Y. A.; Zhou, Z.; Randall, G.; Michalska, K.; Snyder, S. A.; Dickinson, B. C.; Joachimiak, A. Structure of Papain-like Protease from SARS-CoV-2 and Its Complexes with Non-Covalent Inhibitors. *Nat. Commun.* 2021, 12, 1−9.

(23) Nogueira, N.; Barbosa, B.; Rocha, J. B. T. Toxicology and Pharmacology of Synthetic Organoselenium Compounds: An Update. *Arch. Toxicol.* 2021, 95, 1179−1226.

(24) Dalla Tiezza, M.; Ribaudo, G.; Orian, L. Organodiselenides: Organic Catalysis and Drug Design Learning from Glutathione Peroxidase. *Curr. Org. Chem.* 2019, 23, 1381−1402.

(25) Sanmartin, C.; Plano, D.; Palop, J. Selenium Compounds and Apoptotic Modulation: A New Perspective in Cancer Therapy. *Mini Rev. Med. Chem.* 2008, 8, 1020−1031.

(26) Alvarez-Perez, M.; Ali, W.; Marc, M.łg.; Handzlik, J.; Dominguez-Alvarez, E. Selenides and Diselenides: A Review of Their Anticancer and Chemopreventive Activity. *Mol. A J. Synth. Chem. Nat. Prod. Chem.* 2018, 23, 628.

(27) Barbosa, N. V.; Nogueira, C. W.; Nogara, P. A.; de Bem, A. F.; Aschner, M.; Rocha, J. B. T. Organoselenium Compounds as Mimics of Selenoproteins and Thiol Modifier Agents. *Metallomics* 2017, 9, 1703−1734.

(28) Rosa, R.M.; Roesler, R.; Braga, A.L.; Saffi, J.; Henriques, J.A.P. Pharmacology and Toxicology of Diphenyl Diselenide in Several Biological Models. *Braz. J. Med. Biol.* 2007, 40.1287−1304.

(29) Sakurai, T.; Kanayama, M.; Shibata, T.; Itoh, K.; Kobayashi, A.; Yamamoto, M.; Uchida, K. Ebselen, a Seleno-Organic Antioxidant, as an Electrophile. *Chem. Res. Toxicol.* 2006, 19, 1196−1204.

(30) Orian, L.; Toppo, S. Organochalcogen Peroxidase Mimetics as Potential Drugs: A Long Story of a Promise Still Unfulfilled. *Free Rad. Biol. Med.* 66, 2014, 65−74 .

(31) Nogueira, C. W.; Rocha, J. B. T. Diphenyl Diselenide a Janus-Faced Molecule. *J. Braz. Chem. Soc.* 2010, 21, 2055−2071.

(32) Nogara, P. A.; Oliveira, C. S.; Rocha, J. B. T. Chemistry and Pharmacology of Synthetic Organoselenium Compounds. In *Organoselenium Chemistry*; Ranu, B. C., Banerjee, B., Eds.; De Gruyter: Berlin, 2020, pp 305−346.

(33) Oliveira, C. S.; Nogara, P. A.; Ardisson-Araújo, D. M. P.; Aschner, M.; Rocha, J. B. T.; Dórea, J. G. Neurodevelopmental Effects of Mercury. *Adv. Neurotoxicol.* 2018, 27−86.

(34) Singh, B. G.; Gandhi, V. V.; Phadnis, P. P.; Kunwar, A. Identification of Pyridine Derivative of Diselenides as Potent Inhibitor of Main Protease of SARS-CoV-2 through *in silico* Screening and Biochemical Evaluation. *New J. Chem.* 2022, 46, 18447−18457.

(35) Amaral, B. P.; Cargnelutti, J. F.; Mortari, A. P. G.; Merchioratto, I.; Feio, L. M.; Nogueira, C. W.; Weiblen, R.; Flores, E. Diphenyl Diselenide and Cidofovir Present Anti-Viral Activity against Bovine Alphaherpesvirus 2 *in vitro* and in a Sheep Model. *Res. Vet. Sci.* 2021, 134, 78−85.

(36) Benelli, J. L.; Poester, V. R.; Munhoz, L. S.; Melo, A. M.; Trápaga, M. R.; Stevens, D. A.; Xavier, M. O. Ebselen and Diphenyl Diselenide against Fungal Pathogens: A Systematic Review. *Med. Mycol.* **2021**, *59*, 409−421.

(37) Prigol, M.; Schumacher, R. F.; WayneNogueira, C.; Zeni, G. Convulsant Effect of Diphenyl Diselenide in Rats and Mice and Its Relationship to Plasma Levels. *Toxicol. Lett.* **2009**, *189*, 35−39.

(38) Kozikowski, B. A.; Burt, T. M.; Tirey, D. A.; Williams, L. E.; Kuzmak, B. R.; Stanton, D. T.; Morand, K. L.; Nelson, S. L. The Effect of Freeze/Thaw Cycles on the Stability of Compounds in DMSO. *J. Biomol. Screen.* **2003**, *8*, 210−215.

(39) Dludla, P. V.; Jack, B.; Viraragavan, A.; Pheiffer, C.; Johnson, R.; Louw, J.; Muller, C. J. F. A Dose-Dependent Effect of Dimethyl Sulfoxide on Lipid Content, Cell Viability and Oxidative Stress in 3T3-L1 Adipocytes. *Toxicol. Reports* **2018**, *5*, 1014−1020.

(40) Nguyen, S.; Nguyen, S. T.; Truong, H. T.-L.; Truong, K. D. Comparative Cytotoxic Effects of Methanol, Ethanol and DMSO on Human Cancer Cell Lines. *Biomed. Res. Ther.* **2020**, *7*, 3855−3859.

(41) Fintelman-Rodrigues, N.; Sacramento, C. Q.; Ribeiro Lima, C. R.; Souza da Silva, F. S.; Ferreira, A. C.; Mattos, M.; de Freitas, C. S.; Cardoso Soares, V. C.; da Silva Gomes Dias, S.; Temerozo, J. R.; Miranda, M. D.; Matos, A. R.; Bozza, F. A.; Carels, N.; Alves, C. R.; Siqueira, M. M.; Bozza, P. T.; Souza, T. M. L. Atazanavir, Alone or in Combination with Ritonavir, Inhibits SARS-CoV-2 Replication and Proinflammatory Cytokine Production. *Antimicrob. Agents Chemother.* **2020**, *64*, e00825-20.

(42) Sacramento, C. Q.; Fintelman-Rodrigues, N.; Dias, S. S. G.; Temerozo, J. R.; Da Silva, A. de P. D.; da Silva, C. S.; Blanco, C.; Ferreira, A. C.; Mattos, M.; Soares, V. C.; Pereira-Dutra, F.; Miranda, M.; Barreto-Vieira, D. F.; da Silva, M. A. N.; Santos, S. S.; Torres, M.; Chaves, O. A.; Rajoli, R. K. R.; Paccanaro, A.; Owen, A.; Bou-Habib, D. C.; Bozza, P. T.; Souza, T. M. L. Unlike Chloroquine, Mefloquine Inhibits SARS-CoV-2 Infection in Physiologically Relevant Cells. *Viruses* **2022**, *14*, 374.

(43) Laboratory Biosafety Guidance Related to Coronavirus Disease (COVID-19), 2022 https://www.who.int/publications/i/item/laboratory-biosafety-guidance-related-to-coronavirus-disease-(covid-19) (accessed May 25, 2022).

(44) Eberhardt, J.; Santos-Martins, D.; Tillack, A. F.; Forli, S.AutoDock Vina 1.2.0: New Docking Methods, Expanded Force Field, and Python Bindings. *J. Chem. Inf. Model.* **2021**, *61*, 3891−3898.

(45) Trott, O.; Olson, A. J. Improving the Speed and Accuracy of Docking. *J. Comput. Chem.* **2010**, 455−461.

(46) Pettersen, E. F.; Goddard, T. D.; Huang, C. C.; Couch, G. S.; Greenblatt, D. M.; Meng, E. C.; Ferrin, T. E. UCSF Chimera - A Visualization System for Exploratory Research and Analysis. *J. Comput. Chem.* **2004**, *25*, 1605−1612.

(47) Awoonor-Williams, E.; Abu-Saleh, A. A. A. A. Covalent and Non-Covalent Binding Free Energy Calculations for Peptidomimetic Inhibitors of SARS-CoV-2 Main Protease. *Phys. Chem. Chem. Phys.* **2021**, *23*, 6746−6757.

(48) Suárez, D.; Díaz, N. SARS-CoV-2 Main Protease: A Molecular Dynamics Study. *J. Chem. Inf. Model.* **2020**, *60*, 5815−5831.

(49) Case, D. A.; Belfon, K.; Ben-Shalom, I. Y.; Brozell, S. R.; Cerutti, D. S.; Cheatham, T. E. V. W. D. C., III; Darden, T. A.; Duke, R. E.; Giambasu, G.; Gilson, M. K.; Gohlke, H.; Goetz, A. W.; Harris, R. S. I.; Izmailov, S. A.; Kasavajhala, K.; Kovalenko, A.; Krasny, R.; Kurtzman, T.; Lee, T. S.; LeGrand, S.; Li, P.; Lin, C.; Luchko, T.; Luo, R.; Man, V.; Merz, K. M.; Miao, Y.; Mikhailovskii, O.; Monard, G.; Nguyen, H.; Onufriev, A. F.; Pan, S.; Pantano, R.; Qi, D. R.; Roe, A.; Roitberg, C.; Sagui, S.; Schott-Verdugo, J.; Shen, C. L.; Simmerling, N. R.; Skrynnikov, J.; Smith, J.; Swails, R. C.; Walker, J.; Wang, L.; Wilson, R. M.; Wolf, X.; Wu, Y.; Xiong, Y. X.; Kollman, D. M. Y. *AMBER 2020*; University of California: San Francisco, 2020.

(50) Maier, J. A.; Martinez, C.; Kasavajhala, K.; Wickstrom, L.; Hauser, K. E.; Simmerling, C. Ff14SB: Improving the Accuracy of Protein Side Chain and Backbone Parameters from Ff99SB. *J. Chem. Theory Comput.* **2015**, 113696−.

(51) Torsello, M.; Pimenta, A. C.; Wolters, L. P.; Moreira, I. S.; Orian, L.; Polimeno, A. General AMBER Force Field Parameters for Diphenyl Diselenides and Diphenyl Ditellurides. *J. Phys. Chem. A* **2016**, *120*, 4389−4400.

(52) Peters, M. B.; Yang, Y.; Wang, B.; Füsti-Molnár, L.; Weaver, M. N.; Merz, K. M. Structural Survey of Zinc Containing Proteins and the Development of the Zinc AMBER Force Field (ZAFF). *J. Chem. Theory Comput.* **2010**, *6*, 2935−2947.

(53) Jorgensen, W. L.; Chandrasekhar, J.; Madura, J. D.; Impey, R. W.; Klein, M. L. Comparison of Simple Potential Functions for Simulating Liquid Water. *J. Chem. Phys.* **1983**, *79*, 926−935.

(54) Davidchack, R. L.; Handel, R.; Tretyakov, M. V. Langevin Thermostat for Rigid Body Dynamics. *J. Chem. Phys.* **2009**, *130*, 234101.

(55) Berendsen, H. J. C.; Postma, J. P. M.; van Gunsteren, W. F.; DiNola, A.; Haak, J. R. Molecular Dynamics with Coupling to an External Bath. *J. Chem. Phys.* **1984**, *81*, 3684.

(56) Humphrey, W.; Dalke, A.; Schulten, K. VMD: Visual Molecular Dynamics. *J. Mol. Graph.* **1996**, 33−38.

(57) Biovia, D. S.; *Discovery Studio Modeling Environment*; Release, 2017.

(58) Roe, D. R.; Cheatham, T. E. PTRAJ and CPPTRAJ: Software for Processing and Analysis of Molecular Dynamics Trajectory Data. *J. Chem. Theory Comput.* **2013**, *9*, 3084−3095.

(59) Omelyan, I.; Kovalenko, A. Generalised Canonical−Isokinetic Ensemble: Speeding up Multiscale Molecular Dynamics and Coupling with 3D Molecular Theory of Solvation, **2013**, *39*, 25−48 .

(60) Onufriev, A.; Bashford, D.; Case, D. A. Exploring Protein Native States and Large-Scale Conformational Changes with a Modified Generalized Born Model. *Proteins* **2004**, *55*, 383−394.

(61) Chen, F.; Liu, H.; Sun, H.; Pan, P.; Li, Y.; Li, D.; Hou, T. Assessing the performance of the MM/PBSA and MM/GBSA methods. 6. Capability to predict protein-protein binding free energies and re-rank binding poses generated by protein-protein docking. *Phys. Chem. Chem. Phys.* **2016**, *18*, 22129−22139.

(62) Sk, M. F.; Roy, R.; Jonniya, N. A.; Poddar, S.; Kar, P. Elucidating Biophysical Basis of Binding of Inhibitors to SARS-CoV-2 Main Protease by Using Molecular Dynamics Simulations and Free Energy Calculations. *J. Biomol. Struct. Dyn.* **2021**, *39*, 3649−3661.

(63) Oehme, D. P.; Brownlee, R. T. C.; Wilson, D. J. D. Effect of Atomic Charge, Solvation, Entropy, and Ligand Protonation State on MM-PB(GB)SA Binding Energies of HIV Protease. *J. Comput. Chem.* **2012**, *33*, 2566−2580.

(64) Hou, T.; Wang, J.; Li, Y.; Wang, W. Assessing the Performance of the MM/PBSA and MM/GBSA Methods. 1. The Accuracy of Binding Free Energy Calculations Based on Molecular Dynamics Simulations. *J. Chem. Inf. Model.* **2011**, *51*, 69−82.

(65) Miller, B. R.; McGee, T. D.; Swails, J. M.; Homeyer, N.; Gohlke, H.; Roitberg, A. E. MMPBSA.Py: An Efficient Program for End-State Free Energy Calculations. *J. Chem. Theory Comput.* **2012**, *8*, 3314−3321.

(66) Marques, S. M.; Bednar, D.; Damborsky, J. Computational Study of Protein-Ligand Unbinding for Enzyme Engineering. *Front. Chem.* **2019**, *6*, 650.

(67) Frisch, M. J.; Trucks, G. W.; Schlegel, H. B.; Scuseria, G. E.; Robb, M. A.; Cheeseman, J. R.; Scalmani, G.; Barone, V.; Mennucci, B.; Petersson, G. A.; Nakatsuji, H.; Caricato, M.; Li, X.; Hratchian, H. P.; Izmaylov, A. F.; Bloino, J.; Zheng, G.; Sonnenberg, J. L.; Hada, M.; Ehara, M.; Toyota, K.; Fukuda, R.; Hasegawa, J.; Ishida, M.; Nakajima, T.; Honda, Y.; Kitao, O.; Nakai, H.; Vreven, T.; Montgomery, J. A., Jr.; Peralta, J. E.; Ogliaro, F.; Bearpark, M.; Heyd, J. J.; Brothers, E.; Kudin, K. N.; Staroverov, V. N.; Kobayashi, R.; Normand, J.; Raghavachari, K.; Rendell, A.; Burant, J. C.; Iyengar, S. S.; Tomasi, J.; Cossi, M.; Rega, N.; Millam, J. M.; Klene, M.; Knox, J. E.; Cross, J. B.; Bakken, V.; Adamo, C.; Jaramillo, J.; Gomperts, R.; Stratmann, R. E.; Yazyev, O.; Austin, A. J.; Cammi, R.; Pomelli, C.; Ochterski, J. W.; Martin, R. L.; Morokuma, K.; Zakrzewski, V. G.; Voth, G. A.; Salvador, P.; Dannenberg, J. J.; Dapprich, S.; Daniels, A.

D.; Farkas, O.; Foresman, J. B.; Ortiz, J. V.; Cioslowski, J.; Fox, D. J. *Gaussian16 (Revision A.03)*; Gaussian Inc: Wallingford CT, 2016.

(68) Becke, A. D. Density-Functional Thermochemistry. III. The Role of Exact Exchange. *J. Chem. Phys.* **1993**, *98*, 5648−5652.

(69) Raghavachari, K. Perspective on "Density Functional Thermochemistry. III. The Role of Exact Exchange. *Theor. Chem. Acc.* **2000**, *103*, 361−363.

(70) Becke, A. D.; Johnson, E. R. A Density-Functional Model of the Dispersion Interaction. *J. Chem. Phys.* **2005**, *123*, 154101.

(71) Grimme, S. Density Functional Theory with London Dispersion Corrections. *Wiley Interdiscip. Rev. Comput. Mol. Sci.* **2011**, *1*, 211−228.

(72) Marenich, A. V.; Cramer, C. J.; Truhlar, D. G. Universal Solvation Model Based on Solute Electron Density and on a Continuum Model of the Solvent Defined by the Bulk Dielectric Constant and Atomic Surface Tensions. *J. Phys. Chem. B* **2009**, *113*, 6378−6396.

(73) Orian, L.; Mauri, P.; Roveri, A.; Toppo, S.; Benazzi, L.; Bosello-Travain, V.; De Palma, A.; Maiorino, M.; Miotto, G.; Zaccarin, M.; Polimeno, A.; Flohé, L.; Ursini, F. Selenocysteine Oxidation in Glutathione Peroxidase Catalysis: An MS-Supported Quantum Mechanics Study. *Free Radic. Biol. Med.* **2015**, *87*, 1−14.

(74) Dalla Tiezza, M.; Bickelhaupt, F. M.; Flohé, L.; Maiorino, M.; Ursini, F.; Orian, L. A Dual Attack on the Peroxide Bond. The Common Principle of Peroxidatic Cysteine or Selenocysteine Residues. *Redox Biol* **2020**, *34*, 101540.

(75) Bortoli, M.; Torsello, M.; Bickelhaupt, F. M.; Orian, L. Role of the Chalcogen (S, Se, Te) in the Oxidation Mechanism of the Glutathione Peroxidase Active Site. *Chemphyschem* **2017**, *18*, 2990−2998.

(76) Citarella, A.; Scala, A.; Piperno, A.; Micale, N. SARS-CoV-2 M pro: A Potential Target for Peptidomimetics and Small-Molecule Inhibitors. *Biomolecules* **2021**, *11*, 607.

(77) Jin, Z.; Du, X.; Xu, Y.; Deng, Y.; Liu, M.; Zhao, Y.; Zhang, B.; Li, X.; Zhang, L.; Peng, C.; Duan, Y.; Yu, J.; Wang, L.; Yang, K.; Liu, F.; Jiang, R.; Yang, X.; You, T.; Liu, X.; Yang, X.; Bai, F.; Liu, H.; Liu, X.; Guddat, L. W.; Xu, W.; Xiao, G.; Qin, C.; Shi, Z.; Jiang, H.; Rao, Z.; Yang, H. Structure of M pro from SARS-CoV-2 and Discovery of Its Inhibitors. *Nature* **2020**, *582*, 289−293.

(78) Sies, H.; Parnham, M. J. Potential Therapeutic Use of Ebselen for COVID-19 and Other Respiratory Viral Infections. *Free Radic. Biol. Med.* **2020**, *156*, 107.

(79) Weng, Y.; Naik, S.; Dingelstad, N.; Lugo, M. R.; Kalyaanamoorthy, S.; Ganesan, A. Molecular Dynamics and *in silico* Mutagenesis on the Reversible Inhibitor-Bound SARS-CoV-2 Main Protease Complexes Reveal the Role of Lateral Pocket in Enhancing the Ligand Affinity. *Sci. Reports* **2021**, *11*, 7429.

(80) Bortoli, M.; Dalla Tiezza, M.; Muraro, C.; Saielli, G.; Orian, L. The 125Te Chemical Shift of Diphenyl Ditelluride: Chasing Conformers over a Flat Energy Surface. *Molecules* **2019**, *24*, 1250.

(81) Bortoli, M.; Zaccaria, F.; Dalla Tiezza, M.; Bruschi, M.; Fonseca Guerra, C. F.; Bickelhaupt, F.; Orian, L. Oxidation of Organic Diselenides and Ditellurides by H2O2 for Bioinspired Catalyst Design. *Phys. Chem. Chem. Phys.* **2018**, *20*, 20874−20885.

(82) Baldo, M.; Forchioni, A.; Irgolic, K. J.; Pappalardo, G. C. Carbon-13 Spin-Lattice Relaxation and Molecular Motion of Diphenyl Dichalcogenides. *J. Am. Chem. Soc.* **1978**, *100*, 97−100.

(83) Zaccaria, F.; Wolters, L. P.; Fonseca Guerra, C.; Orian, L. Insights on Selenium and Tellurium Diaryldichalcogenides: A Benchmark DFT Study. *J. Comput. Chem.* **2016**, *37*, 1672−1680.